Journal of the European Ceramic Society 38 (2018) 4882–4891

Contents lists available at ScienceDirect

Journal of the European Ceramic Society

journal homepage: www.elsevier.com/locate/jeurceramsoc

Original Article

Thermal stability of nanometric TiC-carbon composites: effects of carbon allotropes and Zr milling impurities

J.P. Ramos[a,b,*], T. Stora[b], A.M.R. Senos[c], P. Bowen[a,*]

[a] Laboratory of Powder Technology, École polytechnique fédérale de Lausanne (EPFL), CH-1015 Lausanne, Switzerland
[b] European Organization for Nuclear Research (CERN), CH-1211 Genève 23, Switzerland
[c] Department of Materials and Ceramics Engineering, Universidade de Aveiro, CICECO, 3810-193 Aveiro, Portugal

ARTICLE INFO

Keywords:
Porous nanocomposites
High temperature applications
Lattice parameters
Solid solution
Zirconium carbide-titanium carbide

ABSTRACT

In the ISOL (Isotope Separator OnLine) method a target at high temperatures (up to 2300 °C), is bombarded with high energy protons in order to produce isotopes through nuclear reactions which are simultaneously extracted from the target, ionized and delivered to physics experiments. Due to the enhanced isotope release properties of nanosized porous materials, titanium carbide-carbon porous nanocomposites have been developed at CERN and tested up to 1500 °C. In the interest of the ISOL application, in this study we extended the range of temperatures up to 1800 °C, to test the sintering hindering capabilities of different carbon allotropes. Carbon black was the most effective with the smallest TiC crystallite size: < 80 nm at 1800 °C. Additionally, using thermodynamic modelling, ex-situ X-ray powder diffraction and in-situ gas phase analysis, we show that there are interesting additional phase and lattice parameter changes due to the ZrO_2 impurities from the attrition milling.

1. Introduction

Radioactive ion beams are used all over the world for nuclear, atomic, solid state and bio-physics studies. ISOLDE (Isotope Separator OnLine DEvice) at the European Organization for Nuclear Research – CERN, has developed beam technologies since its start in 1967, with almost 1000 isotope beams available from 74 chemical elements (from $Z = 2$ to 92) [1]. As schematically represented in Fig. 1, ISOLDE uses the ISOL (Isotope Separator OnLine) method to produce radioactive isotopes where high energy particles, in this case protons at 1.4 GeV, are used to bombard a target to induce nuclear reactions which transmute a fraction of the target material atoms into different isotope elements of a lower mass number [2]. Such isotopes are then trapped in the bulk of the target material and have to diffuse to the surface, evaporate and diffuse through the material porosity to a transfer line (also called effusion) connected to an ion source. Here the isotopes are ionized and shaped into a beam which is then conducted to a mass separator where they are separated according to their mass over charge ratios, with a magnetic field thanks to the Lorentz force. The separated beam is then finally conducted to the experimental setup where it will be used for physics research.

As in the ISOL acronym the process is online, meaning that while the isotopes are produced they are continuously released, ionized, extracted and mass separated to be delivered for physics experiments. In such an extreme environment the target materials are required to have high resistance to radiation damage and high production cross-section of the isotope of interest, to be inert with respect to the isotope to be produced and to have low diffusion and effusion times. Commonly, target materials at ISOLDE are made of metals, oxides or carbides. While the metals are usually in the form of thin foils, the oxides and carbides are in powder or pressed powder form.

The target is heated by applying a current in a tantalum oven using the Joule effect. Usually, to have the highest release efficiency, target operation temperatures are brought close to the material melting point. This brings about material microstructure degradation which is given as the main reason for beam intensity reduction over time. Such degradation is assumed to take place due to the sintering of the target material, bringing changes in porosity and an increase in grain size, which increases diffusion distances. Diffusion times can be reduced by increasing temperature or by reducing the material grain size. However, if no microstructure stabilization mechanisms are employed, reduced operation temperatures have to be used since nano and submicrometric particle materials sinter more readily than conventional ones. Furthermore, in order to produce beams of exotic isotopes (with very short half-lives – down to a few tens of milliseconds), the isotope release times (diffusion and effusion times included) must be below or

* Corresponding author at: European Organization for Nuclear Research (CERN), CH-1211 Genève 23, Switzerland.
E-mail addresses: joao.pedro.ramos@cern.ch (J.P. Ramos), paul.bowen@epfl.ch (P. Bowen).
URL: http://www.joaopedroramos.com (J.P. Ramos).

https://doi.org/10.1016/j.jeurceramsoc.2018.07.002
Received 13 June 2018; Accepted 2 July 2018
Available online 07 July 2018

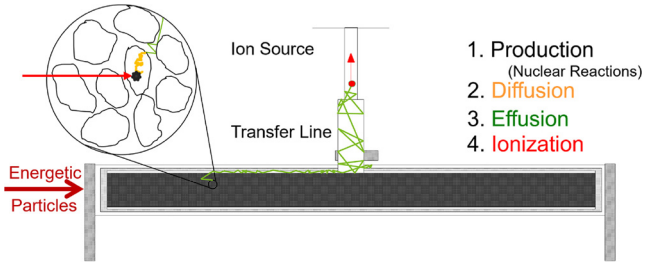

Fig. 1. Schematic representation of the ISOL method steps: production, diffusion, effusion, ionization.

in the same order of magnitude of the isotope half-life. The achievement of such operation parameters is non trivial, requiring the engineering of stable and ultra fine microstructures.

1.1. ISOL target nanomaterials state of the art

It was only during the last decade that special attention has been given to the target material microstructure and its influence in the isotope release efficiency and stability over time [3–8]. Historically, large particles were favored with the justification that smaller particles below 5 µm would sinter too fast and would not provide a stable structure [9].

It was found that by reducing the material particle size of silicon carbide (SiC) from ≈10 to ≈0.6 µm and having high porosity, an increase of a factor of 5 to 10 was seen for magnesium beam intensities due to faster release [3,4]. Consequently, this material is now the standard SiC operated at ISOLDE even though after having been discarded in the past because of its very poor release properties in its micrometric form (≈10 µm) [10].

Calcium oxide (CaO) targets were also known to have unreliable beam intensities and often significantly decreasing over time. This effect was more severe the lower the half-life ($t_{1/2}$), e.g. ^{31}Ar ($t_{1/2}$ = 15.1 ms), ^{32}Ar ($t_{1/2}$ = 98 ms) and ^{35}Ar ($t_{1/2}$ = 1.78 s) intensities were respectively decreased by a factor of ≈5 after of 8, 15 and 90 h, respectively [11]. By synthesizing a nanometric CaO and studying its sintering characteristics [6], stable argon beam intensities with five fold higher intensities over a period of 100 h could be produced despite the low operation temperature needed to avoid material sintering [5].

Uranium carbide targets are usually produced through carbothermal reduction of uranium dioxide with excess graphite. By replacing the graphite carbon source with multi-wall carbon nanotubes (MWCNT) and milling the uranium dioxide down to ≈180 nm a very porous MWCNT and uranium carbide nanocomposite was obtained [12,8]. This target material has shown improved release rates up to a factor of 10 higher without any decrease during operation time for about 8 days. Furthermore the MWCNT hinder sintering so the material can be operated at higher temperatures.

1.2. Titanium-based targets

During the 70s TiC was evaluated, at CERN-ISOLDE, as an unsuitable target material in micrometric powder form (1-50 µm). Both at 2300 °C [9] and when mixed with graphite at 1900 °C [10], there was very little isotope release. Titanium is still used as a target material at ISOLDE in its metallic form, by rolling 25 µm thick foils in a Ta oven. The beam intensities produced from such a configuration, often decay over time due to sintering/melting of the foils when operated higher than 1200 °C. Titanium oxide (TiO_2) has been studied in the form of micrometric fibers and used as a target material at ISOLDE to produce radioactive ion beams. However, they are outperformed by other oxides (such as CaO) [13,14,1].

TiC composite targets are used at TRIUMF-ISAC (ISOL facility in Canada) to produce radioactive isotopes [15–17]. The targets are produced by milling 1:1 in mass ratio 1 and 7 µm TiC particle sizes, followed by slip casting on a graphite foil and sintered up to 1900 °C. The final material is said to have a final size distribution between 1 and 10 µm with TiC layer of 50% nominal density [15].

1.3. Previous work on nanometric TiC

Similarly to other target materials, the reduction and respective stabilization of TiC particle size at high temperatures was attempted for TiC in a previous study [18]. The processing and sintering of nanosized TiC powders and TiC carbon composites was investigated up to 1500 °C. The results showed that when nano-TiC powders were mixed and/or milled with different carbon allotropes – graphite, carbon black and MWCNT – stable porous nanocomposites could be formed, at 1500 °C for at least 10 h. Without the carbon allotropes the nanosized TiC powders sintered to higher densities with significant grain growth and loss of porosity. Interestingly, attrition milled nano TiC showed lower sinterability than the as-received powder. This was hypothesised as being due to ZrO_2 impurities introduced from the milling media during the attrition milling. For the TiC-carbon nanocomposites, the carbon is assumed to act as an inert second phase that reduces the coordination number of TiC and thus hindering the sintering.

To test the suitability of these nanocomposites as ISOL targets, higher temperatures, up to 1800 °C, are investigated here. These higher temperatures are beneficial for isotope release as long as the target microstructure is stable at the defined operation temperature. To this end we study in detail the phase composition and mass losses at these elevated temperatures, not previously reported. Using thermodynamic modelling, ex-situ X-ray powder diffraction, in-situ gas phase analysis, and scanning electron microscopy we show that there are interesting phase changes (including interaction with the ZrO_2 impurities from the attrition milling) and the stability of some of the composites against sintering is sufficient for use as a target material.

2. Materials and methods

2.1. Processing

The processing used for the composites was developed in a previous study [18] and will be only briefly described here. Nanometric TiC was mixed with graphite, carbon black and MWCNT[1], in an attrition mill in isopropanol with 0.5 wt.% polyvinylpyrrolidone, PVP, as a dispersant. The mixtures where then dried, manually deagglomerated, pressed into cylindrical compacts and heat treated at 450 °C in argon to remove the PVP. An in-house built vacuum-oven was used for the high temperature tests, consisting of a thermally shielded tantalum tube ohmically heated. The oven was operated in vacuum (10^{-3} – 10^{-4} Pa) and heat treatments of 10 h at 1500, 1650 and 1800 °C were conducted with ramps of 8 °C min^{-1}. The samples selected for the higher temperature studies were the ones with the best results obtained in our previous investigation [18]. These were 50 vol.% graphite-TiC (50Gr), 50 vol.% carbon black-TiC (50CB), 75 vol.% MWCNT-TiC (75CNTb) and TiC milled with no carbon (TiCm) for comparison. The starting powders characteristics can be found in Table A.2.1 in the supplementary materials.

2.2. Characterization and data handling

Sample dimensions and weights were determined before and after thermal treatment in order to check for mass losses and follow any

[1] TiC – *Goodfellow* (Ref. LS396999/1), 99.9% pure, 80-130 nm; Graphite – *Alfa Aesar*, Ref. 40798, 325 mesh, < 44 µm; Carbon black – *Orion Engineered Carbons*, *Printex A Pulver*, 40 m^2 g^{-1}, 40 nm primary particle size; MWCNT – *Nanocyl*, Ref. NC3100, > 95% purity, 10 nm diameter, 1.5 µm length.

evolution of the geometrical density (ρ). Specific surface area (SSA), pore size volume and pore size distributions below 200 nm, were determined by nitrogen adsorption isotherms in a *Quantachrome eNOVA2200*. The average median pore size, P_S, was determined from the cumulative size distribution. Microstructures were observed in a *Carl Zeiss SMT Σigma* scanning electron microscope (SEM) with an in-lens secondary electron detector. To take into consideration that the composites had different initial values of ρ, SSA and P_S, the relative variation for each sample and sintering condition was determined through the formula:

$$\Delta X/X_0 = (X - X_0)/X_0 \quad (1)$$

where X corresponds to the characteristic after heat treatment (ρ, S or P_S) and X_0 is the characteristic before the heat treatment (ρ_0, S_0 or $P_{S,0}$). The influence of the thermal treatment temperature and carbon allotrope added to TiC were analysed on the variation of SSA – $\Delta S/S_0$, density – $\Delta\rho/\rho_0$ and pore size below 200 nm – $\Delta P_S/P_{S,0}$. A repetition for each test (2 samples) was done and statistical analysis of variance (factorial ANOVA) [19] was carried out – the statistical design schematic can be found in Fig. A.2.1 in the supplementary materials).

X-ray powder diffraction (XRPD) was made using a *PANalytical X'PERT PRO* diffractometer with a X-ray Cu source, with 2θ from 20 to 125° and a 0.013 step size (measurement 98 $s/°2\theta$) for good statistics. The *PANalytical HighScore Plus v4.1* software [20] was used for Rietveld refinement in order to extract lattice parameters and quantify phase ratios. The Williamson-Hall method (W.H.) is used to evaluate both crystallite size (*XS*) and microstrain in the TiC [21]. However, the peaks did not present either a Lorentz shape (linear W.H.) neither a Gaussian shape (quadratic W.H.), they had a contribution from both (Voigt function). Hence, a variation of the W.H. method to account for this proposed by J. Langford [22] was used (hence forward called LWH). The instrumental broadening was determined with a LaB_6 standard material.

Residual gas analysis (RGA) was used in order to study the mass losses of the composite as a function of temperature. A *Pfeiffer Prisma Plus QMA200* quadrupole mass spectrometer (QMS) connected to a *Agilent TPS-mobile TV81* pumping station was used. The samples were heated in a *Carbolite STF 15/450* horizontal alumina tube oven, adapted with in-house made flanges to allow the evacuation of the chamber, via an *Agilent TPS-mobile TV301* pumping station. The QMS was connected to the oven through a small chicane with reduced conductance to reduce the gas supply rate. This was done in order to keep the pressure in the QMS as low as possible as required for its proper function. The oven was heated to 1500 °C, where the QMS was recording a spectrum of the mass number over charge ratio ($1 \leq A/q \leq 100$) every 2 minutes during the 8 °C min^{-1} heating ramp. In addition to the mass spectrum, the pressure was also recorded during the heating ramp, which can be directly correlated with the mass losses ($\Delta m/m_0$). All the results obtained were corrected for the system and crucibles outgassing without any sample.

3. Results and discussion

3.1. Selection of the TiC-C nanocomposite for ISOL application

The ISOL target materials can benefit from the smallest grain size and high porosity (which translates in a high SSA) stable at the highest possible temperature. Table 1 summarizes the referred obtained characteristics and the respective microstructures can be found in Fig. 2, before and after thermal treatments at 1500, 1650 and 1800 °C.

The XRPD measurements were useful to isolate and quantify the TiC crystallite sizes (*XS*) in the composites through peak broadening using the LWH method, as can be seen in Table 1. The value of 51 nm obtained for TiC *XS* is consistent with SEM measured particles (64 ± 29 nm [23]) and with particle size calculated from SSA (48 nm – Table A.2.1 in supplementary materials). Furthermore, good reproducibility of the technique is shown through the consistency of the TiC crystallite size measurements in the as produced composites (TiCm, 50Gr, 50CB, 75CNTb). However, the technique is not as valid for crystallite sizes much larger than 100 nm [24] (e.g. TiCm at 1800 °C in Table 1 – 277 nm) and there is a clear mismatch when comparing with grain sizes obtained in the SEM, which are about 500 nm as seen in Fig. 2d.

Table 1
Density ρ and relative density (ρ_r), SSA, and XRPD determined crystallite size (*XS*) of TiCm, 50Gr, 50CB and 75CNTb as produced and after heat treatments for 10 h at 1500, 1650 and 1800 °C.

		TiC	TiCm	50Gr	50CB	75CNTb
XS (nm)	As produced	51	48	43	43	46
	1500 °C	252	107	59	52	52
	1650 °C	–	122	64	58	47
	1800 °C	–	277	134	76/68[c]	138
ρ (g cm^{-3}) – ρ_r (%)[a]	As produced	2.37 (48%)[b]	2.35 (47%)	1.94 (53%)	1.64 (47%)	1.54 (35%)
	1500 °C	3.61 (73%)[b]	2.55 (51%)	1.88 (50%)	1.69 (46%)	1.95 (41%)
	1650 °C	–	3.27 (66%)	1.91 (51%)	1.77 (48%)	2.27 (47%)
	1800 °C	–	3.85 (78%)	1.99 (53%)	1.91 (53%)	2.70 (57%)
SSA (m^2 g^{-1})	As produced	25.1[b]	29.1	32.8	36.6	49.4
	1500 °C	0.5[b]	2.3	13.0	22.1	23.0
	1650 °C	–	0.3	10.2	19.7	17.4
	1800 °C	–	0.1	7.7	16.7	12.0

[a] ρ_r calculation accounts for ZrO_2/ZrC impurities, carbon densities and mass losses as explained in the next Section (3.2) and in supplementary materials A.2.1.
[b] TiC data extracted from reference [18].
[c] Two TiC based phases formed – see Section 3.3 for more information.

The TiCm shows obvious signs of sintering with an increasing relative density (ρ_r) and reducing SSA for higher temperatures which is also confirmed from the increasing *XS* values (Table 1) and the microstructures in Fig. 2a to d. At 1500 °C, TiC sinters to a great degree more than TiCm, where the *XS* values are, respectively, 252 and 107 nm, in agreement with previous results [18]. This is hypothesized to be either due to the Zr impurities introduced and/or due to the reduction of the agglomerate size of TiCm by milling, which during heat treatment form a stable network of pores which hinders sintering sooner [18].

Throughout this work the results reported for TiCm serve as reference for the deviation induced by each carbon source on the sintering of TiC. All carbon allotropes have a significant effect on the sintering of TiC, as seen from the microstructures of Fig. 2e to p and also with the overall lower ρ_r, *XS* and higher SSA, at the same sintering temperature, when compared with TiCm (Table 1). At 1800 °C, the best carbon allotrope is carbon black where the *XS* is 76 nm, almost 50% lower than in the other two cases, while they all showed similar relative densities (between 50 and 60%). In our previous study, where these carbon composites were thermally treated up 1500 °C, the 75CNTb composite had been selected as the best one at hindering the sintering of TiC [18]. At 1800 °C, Fig. 2, the TiC grains in the 75CNTb and 50Gr grow at higher temperatures, while the microstructures of 50CB show barely any change. This makes the 50CB the best choice as a potential ISOL target material.

3.2. Detailed microstructural and sintering analysis

A more detailed analysis of the microstructural characteristics is made in this subsection by analyzing the evolution of the ρ ($\Delta\rho/\rho_0$ – Fig. 3a), SSA ($\Delta S/S_0$ – Fig. 3b), and P_S ($\Delta P_S/P_{S,0}$ – Fig. 5), as well as a detailed study of the relative porosity below and above 200 nm (Fig. 4).

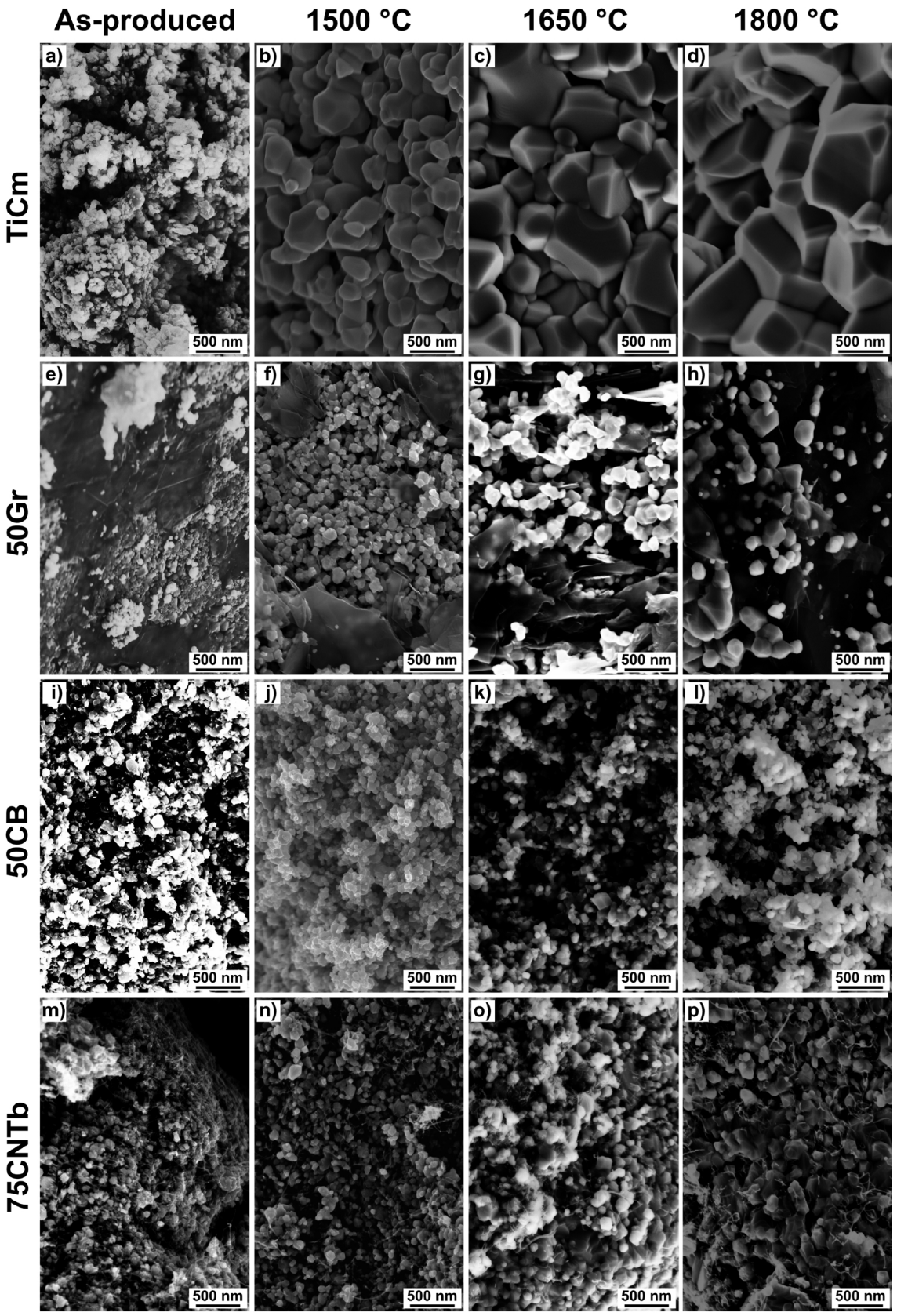

Fig. 2. SEM microstructures of the as produced and thermally treated materials at 1500, 1650 and 1800 °C of TiCm (a to d), 50Gr (e to h), 50CB (i to l) and 75CNTb (m to p).

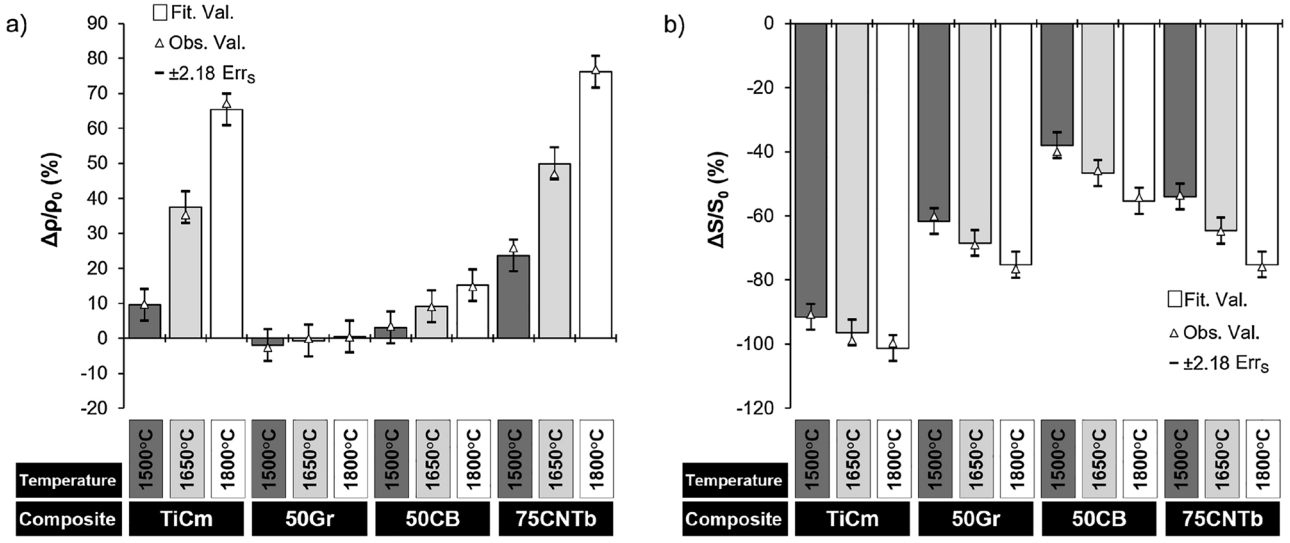

Fig. 3. TiCm, 50Gr, 50CB and 75CNTb $\Delta\rho/\rho_0$ (a) and $\Delta S/S_0$ (b) for heat treatments at 1500, 1650 and 1800 °C for 10 h. The error bars are the standard error of the mean (Err_S) – 95% confidence intervals – for the adjusted values (columns) obtained by ANOVA – analysis of variance.

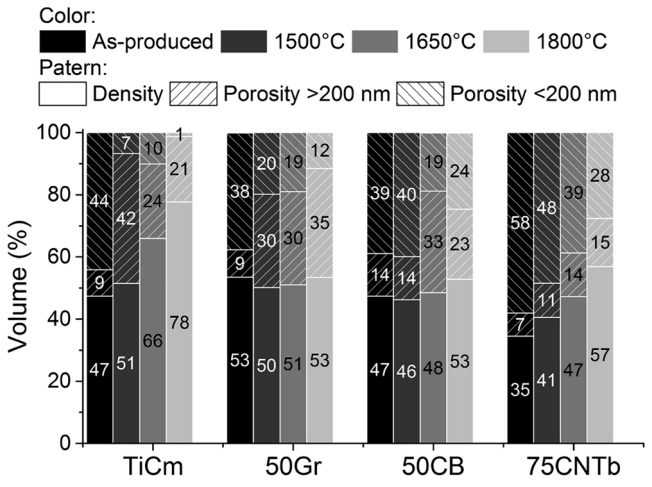

Fig. 4. Relative density and porosity (below and above 200 nm) for the TiCm, 50Gr, 50CB and 75CNTb as produced and heat treated for 10 h at 1500, 1650 and 1800 °C.

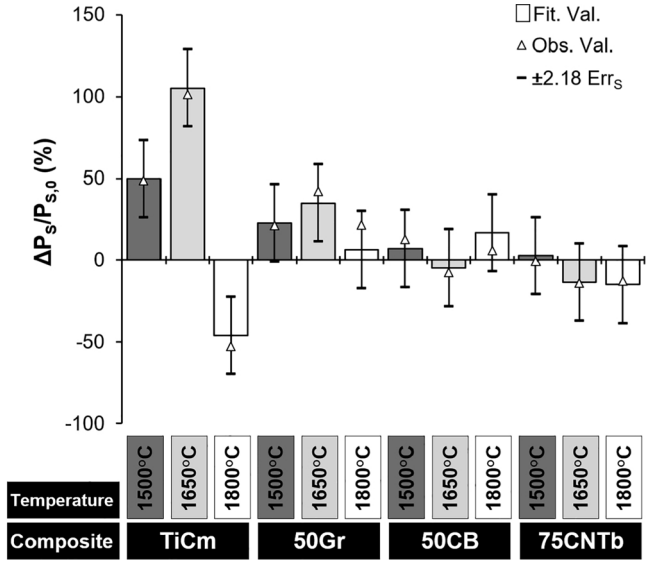

Fig. 5. TiCm, 50Gr, 50CB and 75CNTb $\Delta P_S/P_{S,0}$ for heat treatments at 1500, 1650 and 1800 °C for 10 h. The error bars are the standard error of the mean (Err_S) – 95% confidence intervals – for the adjusted values (columns) obtained by ANOVA – analysis of variance.

The evolution of the characteristics, using ANOVA statistical analysis methods allows a clear representation and interpretation of the complex interactions between these different parameters. In Figs. 3a, b and 5 the characteristic evolution is represented with triangles (Obs. Val.), while the columns represent the ANOVA adjusted values (Fit. Val.) and the error bars, the standard error of the mean for a 95% confidence interval.

For TiCm, as can be seen in Fig. 3a, $\Delta\rho/\rho_0$ values increase for increasing temperature and reaches around 78% of the theoretical value[2] – 4.93 g cm^{-3} – at 1800 °C. In the same figure, the $\Delta\rho/\rho_0$ of 50Gr is barely changing. In 50Gr, the graphite which has large micrometric particles, form a stable non-sinterable skeleton, where only TiC particles in between the graphite grains can sinter, which has a restricted influence on the overall sample density. Continuing the analysis of Fig. 3a, the 50CB densifies more than the 50Gr – $\Delta\rho/\rho_0$ is up to 15% – while the 75CNTb presents the highest values of $\Delta\rho/\rho_0$. The small nanometric carbon black primary particles which are close to the sizes of the TiC (see Table A.2.1 in supplementary materials), blend well with TiC and greatly affect the TiC coordination number, hindering the sintering [18]. However, in the case of 75CNTb, the large density changes are probably related with the carbon mass losses, which very likely partially collapse the very porous structure created by the MWCNT.

$\Delta S/S_0$ values in Fig. 3b for TiCm vary from more than 90 to almost 100%, where in the extreme case of 1800 °C, the SSA decreases from 29.1 to 0.1 m^2 g^{-1}. In the particular case of TiCm heat treated at 1500 °C, in Fig. 3a and b, small $\Delta\rho/\rho_0$, ≈ 9.7% (from 2.35 to 2.55 g cm^{-3} – Table 1) are accompanied by large $\Delta S/S_0$ values, ≈-91% (from 29.1 to 2.1 m^2 g^{-1} – Table 1). In this case, a non-densifying mechanism, such as surface diffusion is likely to be the controlling the sintering, as previously suggested for TiC [18]. Surface diffusion is usually a very important transport mechanism in the early stage sintering, namely for nanomaterials [25,26], bringing an increase in grain size and, from the contribution of secondary densifying mechanisms, a reduced densification.

In Fig. 3b, 50Gr and 75CNTb present the highest $\Delta S/S_0$ of the

[2] For simplicity the ρ_t was assumed not to vary with the TiC stoichiometry.

composites (at 1800 °C, 77 and 76%, respectively) while for 50CB, at the same temperature, $\Delta S/S_0$ was only 54%. As seen in Table 1, the as produced 75CNTb has the highest SSA, followed by 50CB and 50Gr (49.4, 36.6 and 49.4 $m^2 g^{-1}$, respectively), which is due to the carbon allotropes added to the TiC (see Table A.2.1 in supplementary materials). The $\Delta S/S_0$ is a very sensitive sintering parameter, since the growing necks between the TiC particles and grain coarsening phenomena brings large SSA reductions. Despite the influence of mass losses (which will be addressed later), the SSA reductions in Fig. 3b further confirm that carbon black is the most effective at hindering the sintering of TiC.

The relative pore volumes were calculated from the relative density ($\rho_r = \rho/\rho_t$) using the $v_{P,BJH}$ (original values in supplementary materials in Table A.2.2). The porosity fraction with pore size below 200 nm – $P_{r,<200\,nm}$ – and above – $P_{r,>200\,nm}$ – were calculated as well.[3] These are represented in Fig. 4, where TiCm as produced has 53% of porosity, the majority with a size below 200 nm ($P_{r,<200\,nm} = 48\%$). After thermal treatment at 1500 °C, the TiCm density is slightly increased (from 47 to 51%) and accompanied by an increase of the pore size ($P_{r,>200\,nm} = 44\%$). This transformation is explained by the sintering of the nanometric TiC aggregates which, as mentioned above, is probably controlled by surface diffusion, bringing coarsening of the particles with reduced densification. Beyond 1500 °C, the approximate ratio between $P_{r,>200\,nm}$ and $P_{r,<200\,nm}$ is similar while the total porosity keeps reducing as the density increases. The relative evolution of pores below 200 nm ($\Delta P_S/P_{S,0}$) can be seen in Fig. 5 (values of pore sizes below 200 nm can be found in SM in Table A.2.1). $\Delta P_S/P_{S,0}$ is positive for 1500 °C, doubles for 1650 °C and gets negative for 1800 °C. As discussed before, for 1500 and 1650 °C, there is mainly sintering of agglomerates eliminating the small intra-agglomerate pores ($P_{r,<200\,nm}$). Since coarsening is in place, an increase of the porosity between the aggregates is expected [27], so the global pore size increases, whereas for the highest temperature of 1800 °C densification of the microstructure among the agglomerates occurs, bringing simultaneously reduction of porosity and pore size.

The values of $\Delta P_S/P_{S,0}$ for the composites, in Fig. 5, do not present any significant changes within the error (95% confidence interval). It can be interpreted as no pore size changes below 200 nm, which can be attributed to the TiC sintering hindering by the carbons. When considering the pore volumes in Fig. 4, the nanocomposites, except for 50Gr, keep higher $P_{r,<200\,nm}$ than $P_{r,>200\,nm}$, opposite to TiCm, even at 1800 °C. For 75CNTb the $P_{r,<200\,nm}$ is likely to be dominated by the MWCNT small porosity, while in the case of 50Gr, since the graphite has a small $v_{P,BJH}$ (Table A.2.1 in supplementary materials), the main contribution to the $P_{r,<200\,nm}$ comes from the TiC. Although in all composites there is some evolution of $P_{r,<200\,nm}$ to $P_{r,>200\,nm}$ this is not as high as in the case of TiCm. Sintering of TiC will bring densification and/or increase of the $P_{r,>200\,nm}$ relatively to $P_{r,<200\,nm}$, since carbon doesn't sinter.

3.3. Phase evolution

Mass losses ($\Delta m/m_0$) at the end of each thermal cycle for each sample were seen for all samples and were analyzed using ANOVA (Fig. 6). The analysis shows a clear increase of $-\Delta m/m_0$ with temperature for all cases which is related to favorable thermodynamic conditions for carbon burning (Boudouard reaction, $C + CO_2(g) \rightleftharpoons 2CO(g)$). In TiCm, the free carbon comes from the raw material and the carbonaceous deposit from the PVP decomposition during processing.

In order to clarify the origins of the mass losses and check for phase evolution, XRPD and evolved gas phase analysis were made. ZrO_2 is found in all milled materials, typical example for 50Gr in Fig. 7, with

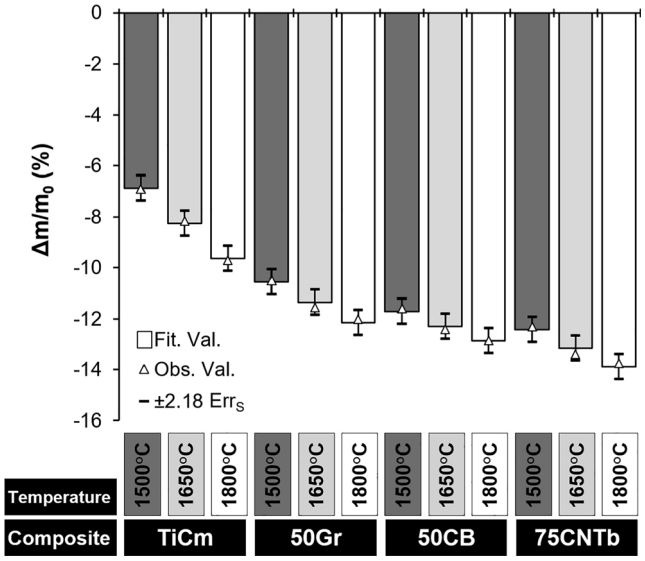

Fig. 6. Mass losses ($\Delta m/m_0$) of TiCm, 50Gr, 50CB and 75CNTb for heat treatments at 1500, 1650 and 1800 °C for 10 h. The error bars are the standard error of the mean (Err_S) – 95% confidence intervals – for the adjusted values (columns) obtained by ANOVA – analysis of variance.

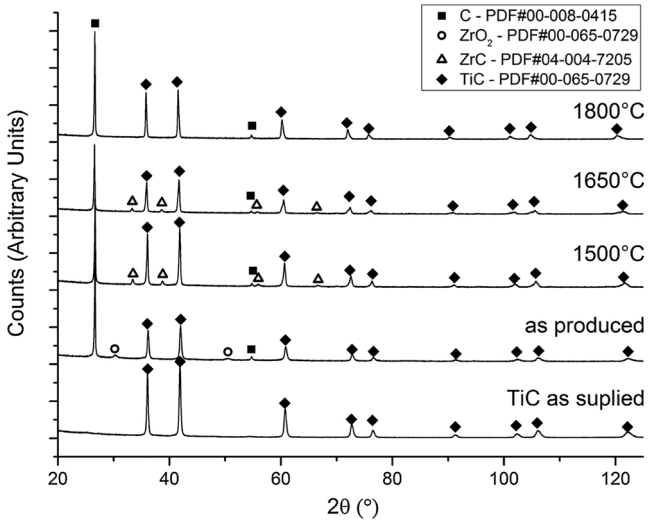

Fig. 7. Diffractograms obtained through XRPD for the TiC as supplied and 50Gr as-produced and heat treated for 1500, 1650 and 1800 °C.

quantities estimated from the XRPD results, varying from 2.6 to 5.7 wt. %, (Table 2). This contamination arises from the milling media and, during the thermal treatments, reacts with carbon producing ZrC, as detected in the 1500 °C diffractogram. At 1650 °C, the ZrC peaks are still present but reduced in intensity and at 1800 °C they disappear completely, which will be discussed in the next subsection.

The residual gas analysis (RGA) was made as a function of temperature up to 1500 °C. All of the carbon composites showed similar behaviour (A.2.2 SM) and a typical result is illustrated for 50CB in Fig. 8. In this figure, the ion current in [A] is shown in log scale as a function of temperature and atomic mass number over charge ratio, A/q, from 1 to 100. The pressure, proportional to the mass losses, as a function of temperature can also be seen. The RGA allows the identification of the temperatures at which certain volatile compounds are released from the samples. Since $q = +1$ are the most probable charge state, A/q values of 44 – CO_2, 32 – O_2, 28 – CO (or N_2 – not really expected) and 18 – H_2O were followed, where the rest, below $A/q = 50$ are either isotope combinations of the referred molecules (such as ^{12}CO

[3] The calculation method was also used as in [18] and is reproduced in supplementary materials A.2.1 of this publication.

Table 2
Stress determined by XRPD using the LWH method, lattice parameters and phase ratios determined from Rietveld refinement of the XRPD diffractograms.

Composite	Temperature (°C)	Stress (%)	Unit cell (Å)	ZrO_2 (wt.%)	ZrC (wt.%)	TiC (wt.%)	C (wt.%)
TiC	As supplied	0.25	4.315	–	–	100	–
	1500	0.01	4.310	–	–	100	–
TiCm	As produced	0.26	4.316	4.3[b]	– [b]	95.7	–
	1500	0.02	4.323	– [b]	– [b]	100	–
	1650	0.03	4.324	– [b]	– [b]	100	–
	1800	0.02	4.322	– [b]	– [b]	100	–
50Gr	As produced	0.20	4.316	5.7	–	66.8	27.4
	1500	0.16	4.323	–	3.4	72.4	24.2
	1650	0.30	4.326	–	1.1	49.5	49.4
	1800	0.23	4.355	–	–	64.8	35.1
50CB	As produced	0.20	4.313	5.7	–	68.5	25.8
	1500	0.10	4.322	–	4.1	80.3	15.6
	1650	0.12	4.325	–	1.1	61.2	37.7
	1800	0.22/ 0.11[a]	4.361/ 4.330[a]	–	–	48.3/ 44.3[a]	7.8
75CNTb	As produced	0.26	4.316	2.6	–	87.1	10.3
	1500	0.10	4.321	–	1.3	89.8	–
	1650	0.20	4.336	–	–	100	–
	1800	0.07	4.340	–	–	100	–

[a] Sample presented phase demixing with two TiC phases. More information in the text.
[b] Energy-dispersive X-ray spectroscopy (EDS) reveals the presence of Zr in 4.4 ± 0.4 wt.% in all samples.

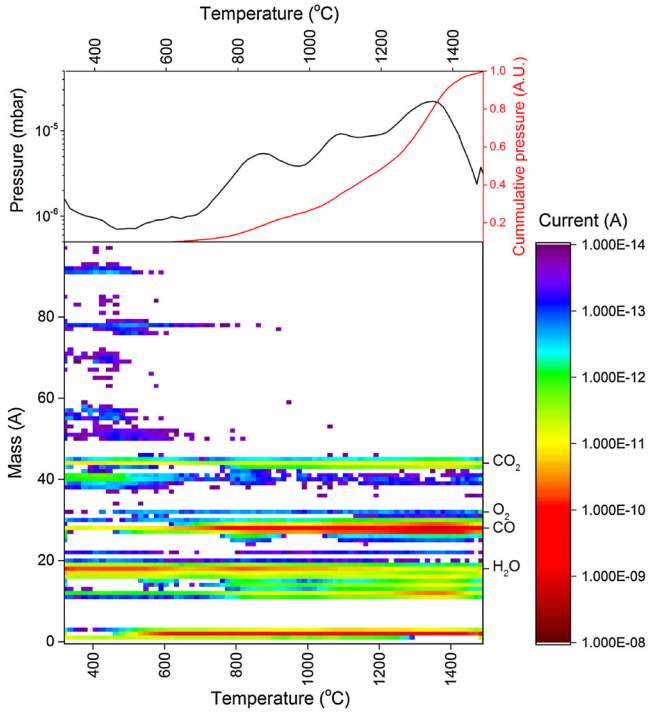

Fig. 8. Mass spectrum shown in mass ($1 \leq A \leq 100$) vs. ion current, obtained by residual gas analysis of 50CB from 350 to 1500 °C (a – bottom) and respective pressure evolution over temperature (a – top).

and ^{13}CO), fragments due to molecular breakup, higher charge states ($q = +2$) or minor leaks in the system. Above $A/q = 50$, the fragments are likely from decomposed PVP which wasn't fully removed from the sample at 450 °C. At temperatures > 600 °C, CO represents most of the gases released from the sample when compared with the intensities

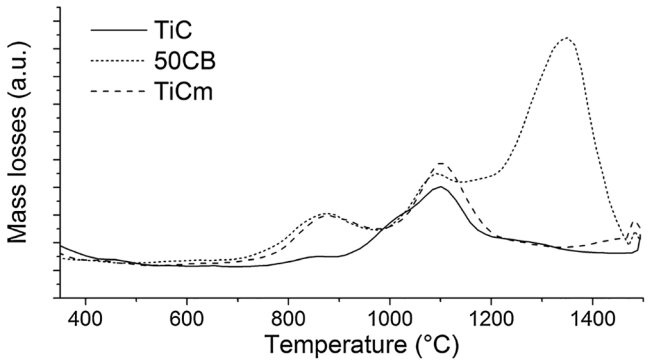

Fig. 9. Mass losses evolution with temperature extracted the RGA pressure evolution for TiC, TiCm and 50CB for comparison.

obtained for other masses. CO_2 is not expected in large quantities, even if it is produced, since the Boudouard reaction is spontaneous at $T > 700$ °C.

Since most of the volatiles released from the samples are CO gas, the pressure for TiC, TiCm and 50CB (50Gr and 75CNTb were very similar to 50CB) are plotted as function of temperature, in Fig. 9. The first peak is seen at 870 °C, the second at 1100 °C and a third at 1400 °C (only seen for 50CB). The first peak is attributed to the reaction of carbon burning either from the free carbon present in the TiC raw material and/or that resulting from the PVP decomposition – which leaves a carbonaceous deposit on the TiC when carried out in an inert atmosphere. X-ray photoelectron spectroscopy (XPS) showed 17.4 wt.% of oxygen, in the as supplied TiC. Since no TiO_2 was identified in XRPD it can be concluded that TiO_2 is probably present in very low quantities and at the surface of the particles in a poorly crystalline form. The second peak at 1100 °C, which was seen in all cases, is possibly the conversion of TiO_2 into TiC (as seen in Fig. 8), through the reaction $TiO_2 + 3C \rightarrow TiC + 2CO(g)$. The third peak at 1400 °C is attributed to the reaction of ZrO_2 with carbon in the composites forming zirconium carbide (ZrC), (as seen in Fig. 8), through the reaction $ZrO_2 + 3C \rightarrow ZrC + 2CO(g)$.

Thermodynamic phase stability diagrams were computed using *HSC 7.11 Chemistry Software* [28] for Ti-C-O and Zr-C-O at 1200 °C and are shown in Fig. 10 (other temperatures are shown in Fig. A.2.3 in supplementary materials), showing the domain of stability of TiC and ZrC in equilibrium with a range of P_{CO} and P_{O_2}. From the conversion of ZrO_2

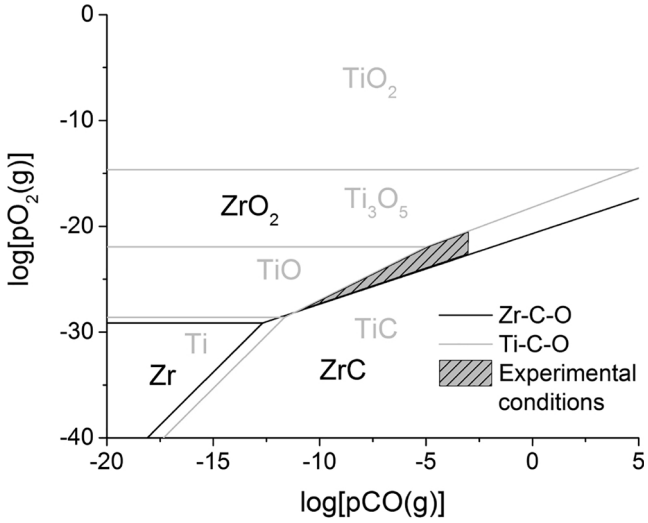

Fig. 10. Thermodynamic Ti–C–O (black) and Zr–C–O (grey) overlapped phase stability diagrams at 1200 °C, showing the calculated range of CO and O_2 partial pressures in the experimental setup: $P_{CO} = 10^{-3} = 10^{-3}$ to 10^{-11} atm and $P_{O_2} = 10^{-28}$ to 10^{-20} atm.

Table 3
C, N and O concentrations in TiC and TiC thermally treated at 1500 °C determined by combustion with infrared adsorption spectrometry and carrier gas hot extraction analysis.

	As supplied	1500 °C
C (at.%)	40.55	40.46
O (at.%)	4.54	0.04
N (at.%)	0.06	0.07
Ti (at.%)	54.77	59.33
C/Ti	0.74	0.68

into ZrC which only starts above about 1200 °C (main peak of gas release curve), the approximate oven atmosphere conditions can be evaluated for O_2 and CO partial pressures, as marked in Fig. 10: $P_{CO} = 10^{-11}$ to 10^{-3} atm and $P_{O_2} = 10^{-28}$ to 10^{-20} atm. The upper limit for $P_{CO} = 10^{-3}$, 10^{-3} atm, is an approximation and is limited by the vacuum system.

3.4. TiC lattice parameters

The broad range of possible composition of TiC_x where $0.5 \leq x \leq 1$, is associated with a considerable variation in the lattice parameter as a function of x [29–31]. In the literature [29,30] the TiC_x lattice (a) is minimum for $TiC_{0.5}$ where $a = 4.299$ Å, increases up to $TiC_{0.85}$ where $a = 4.331$ Å and decreases slightly in stoichiometric TiC, down to $a = 4.326$ Å. At $TiC_{0.85}$, where a is the highest, the melting point is also the highest (3067 °C). It is also known that very low contamination of O and N, decreases the TiC lattice considerably (e.g. up to ≈0.25 wt.% of O, can decrease a up to ≈0.008 Å) [30]. In order to determine C, N and O concentrations in TiC, combustion with infrared adsorption spectrometry [32] was used for C, and carrier gas hot extraction analysis [33] for N and O. The results of these analysis can be seen in Table 3, where Ti quantity was deduced from C, N and O concentration, assuming no other contamination.

A lattice reduction from 4.315 to 4.310 Å between the as-supplied to the thermally treated sample (Table 2), is consistent with the oxygen decrease in Table 3. The decrease of the C/Ti ratio seen in Table 3 confirms the free carbon present in the sample which burns at low temperatures, 870 °C in the mass losses (Fig. 9). The C/Ti ratio considered for TiC was the one of the TiC sample thermally treated at 1500 °C, 0.68 from Table 3. The TiC lattice parameter determined in this work, $a = 4.310$ Å, is slightly lower than that of $a = 4.324$ Å predicted by Storms et al. [30] for $TiC_{0.68}$, which can be attributed to the O and N contamination in the sample.

XRPD analysis of the composites revealed a small gradual shift across all TiC peak positions (Fig. 11) which was inversely proportional to the amount of ZrC phase present in the XRPD. The TiC {111} reflection is represented for TiCm, 50CB and 50Gr where 50Gr presents an intense carbon peak which conveniently serves as an internal standard. Rietveld refinement was conducted to all samples in order to quantify the lattice parameter change. In all cases (Table 2), there is an increase of the lattice parameter from around 4.315 Å (as supplied TiC) to a maximum of 4.361 Å for 50CB, 4.355 Å for 50Gr and 4.340 Å for 75CNTb. In solid solutions the host species can be distorted when there is a significant difference between the solid solution atoms radii: in our case Ti, 1.40 Å, and Zr, 1.55 Å [34]. It can also be seen that in the samples, like 75CNTb, where lower amounts ZrO_2 was present, lower lattice distortions were observed. Also the ZrC dissolution into the TiC lattice seems to be diffusion limited, since only at 1800 °C do the ZrC XRD peaks disappear.

The XRPD peak position shift for 50CB is also shown in Fig. 11 where at 1800 °C the peak transforms into a doublet of similar intensity (inset Fig. 11). The TiC-ZrC phase diagram [35], shows that ZrC forms a continuous solid solution with TiC ($Ti_{(1-x)}Zr_xC$). At low temperatures this solid solution presents an immiscibility asymmetric dome, where

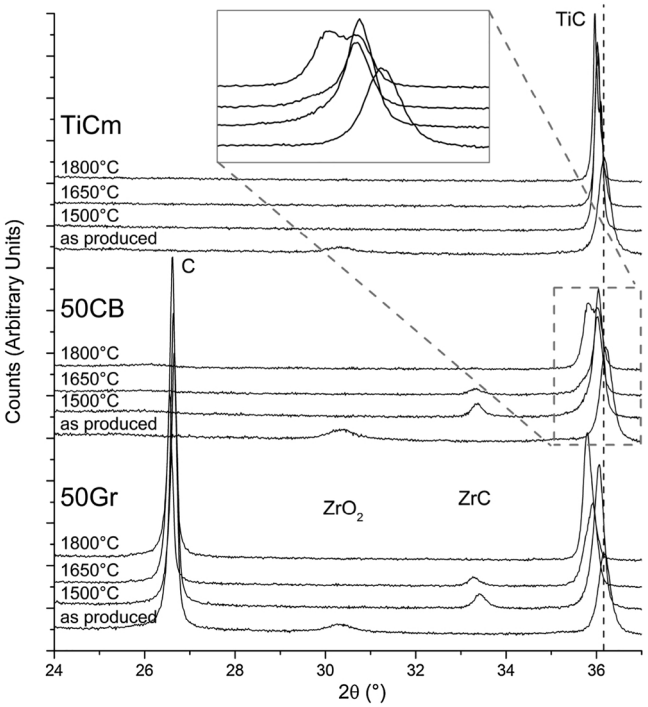

Fig. 11. Diffractograms obtained through XRPD for the TiCm and 50Gr as-produced and heat treated for 1500, 1650 and 1800 °C revealing the TiC peaks shift for higher temperatures, here shown only for TiC {111} reflection.

the solid solution segregates into two phases – one richer than the other in ZrC. For this to happen, ZrC has to be higher than 4-5 at.% in TiC, which only happens for 50Gr and 50CB. The lower 50Gr mixture homogeneity, due to the different particle sizes of TiC and graphite, probably doesn't allow sufficient contact between the ZrC and TiC phases, bringing the local ZrC/TiC ratio down. Phase segregation in the TiC-ZrC system was seen in the study of Li et al. [35] for $Ti_{0.80}Zr_{0.20}C$ where a higher lattice ZrC-rich phase (a = 4.68 Å) and a lower lattice TiC-rich phase (a = 4.35 Å) were formed. The same seems to be happening here, with lower Zr content, where a lattice of 4.361 Åwas found for the phase with a higher ZrC content and the other with 4.330 Å– with less ZrC.

The Vegard's law [36] is an empirical law used to predict the lattice of a solid solution, $A_{1-x}B_x$ of phases A and B, originally in ionic salts:

$$a_{A_{1-x}B_x} = (1 - x)a_A + xa_B \quad (2)$$

where a_A and a_B are the lattice parameter of the component A and B respectively, x is the at.% of B in A and $a_{A_{1-x}B_x}$ is the lattice parameter for the solid solution. Using the Vegard's law for the TiCm case, which is $Ti_{0.976}Zr_{0.024}C$ (c.a. from TiCm as produced, Table 2) a lattice parameter of 4.319 Å is found, a value in very good agreement with the one experimentally obtained, $a = 4.323$ Å. Using the lattice parameter obtained for TiC ($a = 4.310$ Å in this work, Table 2) and $a = 4.698$ Å for ZrC [29], the Vegard's law predicts a lattice of 4.329 Å for 50Gr where its TiC is in fact $Ti_{0.96}Zr_{0.04}C$. In our case a value of 4.355 Å was obtained (Table 2), which is significantly higher than the theoretically predicted one. We believe that this lattice increase is due to the excess carbon, being dissolved into TiC which is known to increase its lattice parameter [30].

In Fig. 12, the a value measured for 1800 °C is plotted for all the composites, as well as the predicted one by the Vegard's Law, assuming that the TiC remains as $TiC_{0.68}$ or it increases to $TiC_{0.85}$ – the value with the highest lattice parameter. The calculated values were determined using the measured TiC lattice in the case of $TiC_{0.68}$ and the one reported in the literature for $TiC_{0.85}$ [30], where the ZrC amount was determined from XRPD. As seen in Fig. 12 the calculated lattice

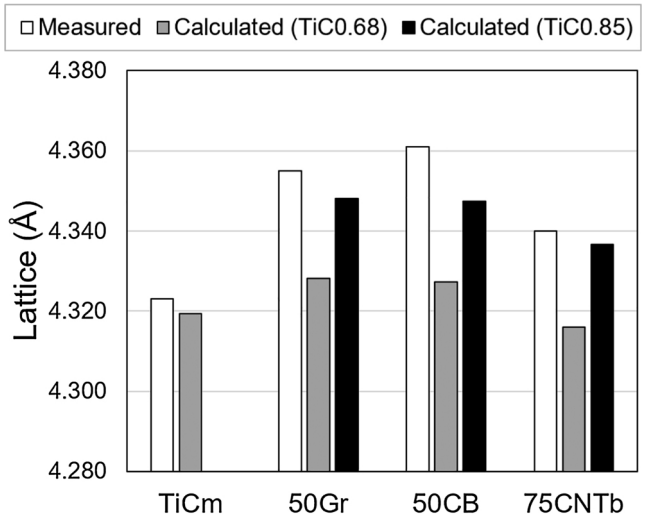

Fig. 12. Lattice parameters of TiC measured for 1800 °C using Rietveld refinement of the XRPD patterns and calculated for ZrC solubility using the Vegard's law, for different Ti-C ratios – $TiC_{0.68}$ and $TiC_{0.85}$ – for TiCm, 50Gr, 50CB and 75CNTb.

parameter, assuming $TiC_{0.85}$, is much closer to the experimental value, which confirms that the TiC has changed its stoichiometry. Similarly, calculations have been done by Li et al. [35], and the calculated lattice parameters for $Ti_{0.80}Zr_{0.20}C$ were relatively close to the one predicted by equation (2). In our case, the increased lattice parameter of the TiC may bring benefits for the application in view, since the melting point of TiC is at its highest (3067 °C) with $TiC_{0.85}$ [30] (ca. 2997 °C for $TiC_{0.68}$), which should also contribute in the delay of sintering at higher temperatures.

In the case of TiCm, the ZrC disappears after 1500 °C and no clear RGA signal for ZrO_2 transformation into ZrC was seen in Fig. 9. Energy-dispersive X-ray spectroscopy (EDS) revealed the same quantity of Zr in all TiCm samples (as produced and thermally treated), 4.4 ± 0.4 wt.%, showing that Zr is still present in the samples. The XRPD systematic peak shift for higher temperatures for TiCm (Fig. 11) is less evident than for the TiC-C composites. The TiC lattice parameter increase at 1500 °C is seen similarly to the TiC-C composites, however its *a* value does not change at higher temperatures. Here, the Zr from the ZrO_2 is probably being introduced into the TiC, at a slower rate due to the lack of carbon. Furthermore, the ZrO_2 reduction to ZrC is not indicated in the RGA, which does not have a 10 h dwell time as the samples have, supporting the incorporation hypothesis.

In Table 2 the lattice stress values are also presented. Lattice strain can be divided in two categories: uniform strain and nonuniform strain [37]. Uniform strain is caused by uniform changes in *d* spacing, causing a shift in the peak position, such as the solid solutions discussed before. The nonuniform strain is usually due to imperfections in the lattice such as defects, which broaden the peaks and reduce the intensities. By looking at Table 2, the initial TiC material has already some degree of strain (0.25%) probably from the production method used (which usually involve milling). As expected for the TiC without any additive, the strain in Table 2, is reduced during heat treatments, since the defects are annealed. This does not happen for any of the composites when heat treated at high temperatures. Both types of strain are present in the TiC-C nanocomposites: uniform strain due to the incorporation of Zr in the TiC lattice and nonuniform strain which may arise from the sintering stresses [37] due to the constrained sintering of the TiC.

4. Conclusions

Nanometric titanium carbide was successfully stabilized up to 1800 °C with addition of 3 different carbon allotropes: graphite, carbon black and MWCNT. The most effective carbon allotrope hindering the sintering of TiC was carbon black, followed by MWCNT and graphite. After heat treatment at 1800 °C, the TiC crystallite sizes without any carbon addition were more than 500 nm while for 50 vol.% carbon black-TiC (50CB), 50 vol.% graphite-TiC (50Gr) and 75 vol.% MWCNT (bulk density)-TiC (75CNTb) the crystallite sizes were 76, 134 and 138 nm, respectively. A relative density of 78% was obtained for TiC sintered at 1800 °C whereas the composites attained significantly lower densities: 55% for both 50CB and 50Gr and 58% for 75CNTb.

The composites processing route introduces a ZrO_2 contamination (from 2.6 to 5.7 wt.%) that comes from the milling elements. This contamination converts, at about 1400 °C, to ZrC consuming carbon of the nanocomposites and releasing CO gas. The ZrC phase gradually solubilizes into the TiC lattice, and at 1800 °C no more ZrC is detected by X-ray powder diffraction. Simultaneously, the lattice parameter of TiC increases from 4.315 nm up to 4.361 nm, due to the ZrC solubilization. When comparing the sintering behavior of the TiCm (containing Zr) and the produced nanocomposites, it can be concluded that although the contamination with Zr and lattice increase of TiC (due to C incorporation) contribute to the hindering of the TiC sintering, carbon addition is the controlling factor which reduces the coordination number of the TiC grains.

All of the produced carbon composites, even after being heated up to 1800 °C, fulfill the microstructural requirements for ISOL target application (high porosity and nanometric particle size) ensuring smaller diffusion lengths and faster effusion of isotopes from the TiC.

Acknowledgements

The authors would like to acknowledge Carlos Morais for the technical expertise with the attrition milling and during experimental work, Maria João Bastos and Artur Sarabando for the XRPD tests, Nicolas Xanthopoulos for the XPS tests. We acknowledge Prof. Jacques Lemaître for the ANOVA – analysis of variance – calculation tools and Prof. Heinrich Hofmann for the interesting phase diagrams discussions. We would like to acknowledge as well Orion Engineered Carbons, S.A. for supplying the carbon black for this study. The author J.P. Ramos gratefully acknowledge CERN and EPFL for the doctoral studentship funding.

Appendix A. Supplementary data

Supplementary data associated with this article can be found, in the online version, at https://doi.org/10.1016/j.jeurceramsoc.2018.07.002.

References

[1] ISOLDE-CERN, ISOLDE Yield Database. http://test-isolde-yields.web.cern.ch/test-isolde-yields/query_tgt.htm.
[2] R. Catherall, W. Andreazza, M. Breitenfeldt, A. Dorsival, G.J. Focker, T.P. Gharsa, T.J. Giles, J.-L. Grenard, F. Locci, P. Martins, S. Marzari, J. Schipper, A. Shornikov, T. Stora, The ISOLDE facility, J. Phys. G: Nucl. Part. Phys. 44 (9) (2017) 094002, https://doi.org/10.1088/1361-6471/aa7eba.
[3] S. Fernandes, Submicro- and Nano-Structured Porous Materials for Production of High-Intensity Exotic Radioactive Ion Beams, École polytechnique fédérale de Lausanne, 2010, https://doi.org/10.5075/epfl-thesis-4813 (PhD Thesis).
[4] T. Stora, Recent developments of target and ion sources to produce ISOL beams, Nucl. Instrum. Methods Phys. Res. Sect. B: Beam Interact. Mater. Atoms 317 (2013) 402–410, https://doi.org/10.1016/j.nimb.2013.07.024.
[5] J. Ramos, A. Gottberg, T. Mendonça, C. Seiffert, A. Senos, H. Fynbo, O. Tengblad, J. Briz, M. Lund, G. Koldste, M. Carmona-Gallardo, V. Pesudo, T. Stora, Intense $^{31-35}$Ar beams produced with a nanostructured CaO target at ISOLDE, Nucl. Instrum. Methods Phys. Res. Sect. B: Beam Interact. Mater. Atoms 320 (2014) 83–88, https://doi.org/10.1016/j.nimb.2013.12.009.
[6] J. Ramos, C. Fernandes, T. Stora, A. Senos, Sintering kinetics of nanometric calcium oxide in vacuum atmosphere, Ceram. Int. 41 (6) (2015) 8093–8099, https://doi.org/10.1016/j.ceramint.2015.03.007.
[7] J. Ramos, A. Gottberg, R. Augusto, T. Mendonca, K. Riisager, C. Seiffert, P. Bowen, A. Senos, T. Stora, Target nanomaterials at CERN-ISOLDE: synthesis and release data, Nucl. Instrum. Methods Phys. Res. Sect. B: Beam Interact. Mater. Atoms 376

(2016) 81–85, https://doi.org/10.1016/j.nimb.2016.03.003.
[8] A. Gottberg, Target materials for exotic ISOL beams, Nucl. Instrum. Methods Phys. Res. Sect. B: Beam Interact. Mater. Atoms (2016), https://doi.org/10.1016/j.nimb.2016.01.020.
[9] L. Carraz, I. Haldorsen, H. Ravn, M. Skarestad, L. Westgaard, Fast release of nuclear reaction products from refractory matrices, Nucl. Instrum. Methods 148 (2) (1978) 217–230, https://doi.org/10.1016/0029-554X(70)90171-0.
[10] P. Hoff, O. Jonsson, E. Kugler, H. Ravn, Release of nuclear reaction products from refractory compounds, Nucl. Instrum. Methods Phys. Res. 221 (2) (1984) 313–329, https://doi.org/10.1016/0167-5087(84)90002-4.
[11] J. Ramos, Effect of Calcium Oxide Microstructure on the Diffusion of Isotopes, University of Aveiro, 2012 (Master thesis), http://cdsweb.cern.ch/record/1425438/.
[12] A. Gottberg, et al. Development and Online Tests of a Nano-Structured Uranium Carbide – MWCNT Composite for the Production of Rare Isotope Beams at ISOLDE-CERN (in preparation).
[13] K. Peräjärvi, U. Bergmann, V. Fedoseyev, A. Joinet, U. Köster, C. Lau, J. Lettry, H. Ravn, M. Santana-Leitner, Studies of release properties of ISOLDE targets, Nucl. Instrum. Methods Phys. Res. Sect. B: Beam Interact. Mater. Atoms 204 (2003) 272–277, https://doi.org/10.1016/S0168-583X(02)01924-9.
[14] U. Köster, U. Bergmann, D. Carminati, R. Catherall, J. Cederkäll, J. Correia, B. Crepieux, M. Dietrich, K. Elder, V. Fedoseyev, L. Fraile, S. Franchoo, H. Fynbo, U. Georg, T. Giles, A. Joinet, O. Jonsson, R. Kirchner, C. Lau, J. Lettry, H. Maier, V. Mishin, M. Oinonen, K. Peräjärvi, H. Ravn, T. Rinaldi, M. Santana-Leitner, U. Wahl, L. Weissman, Oxide fiber targets at ISOLDE, Nucl. Instrum. Methods Phys. Res. Sect. B: Beam Interact. Mater. Atoms 204 (2003) 303–313, https://doi.org/10.1016/S0168-583X(03)00505-6.
[15] M. Dombsky, H. V., Method of forming composite ceramic targets, Patent no. US 7, 682,664 B2 (2010).
[16] V. Hanemaayer, P. Bricault, M. Dombsky, Composite ceramic targets for high power proton irradiation, Nucl. Instrum. Methods Phys. Res. Sect. B: Beam Interact. Mater. Atoms 266 (19–20) (2008) 4334–4337, https://doi.org/10.1016/j.nimb.2008.05.094.
[17] TRIUMF-ISAC, TRIUMF-ISAC Yield Database. http://mis.triumf.ca/science/planning/yield/target.
[18] J. Ramos, A. Senos, T. Stora, C. Fernandes, P. Bowen, Development of a processing route for carbon allotrope-based TiC porous nanocomposites, J. Eur. Ceram. Soc. 37 (13) (2017) 3899–3908, https://doi.org/10.1016/j.jeurceramsoc.2017.04.016.
[19] D.C. Montgomery, Design and Analysis of Experiments, 8th ed., John Wiley & Sons Inc., 2012.
[20] T. Degen, M. Sadki, E. Bron, U. König, G. Nénert, The HighScore suite, Powder Diffract. 29 (S2) (2014) S13–S18, https://doi.org/10.1017/S0885715614000840.
[21] G. Williamson, W. Hall, X-ray line broadening from filed aluminium and wolfram, Acta Metall. 1 (1) (1953) 22–31, https://doi.org/10.1016/0001-6160(53)90006-6.
[22] J. Langford, The use of the Voigt function in determining microstructural properties from diffraction data by means of pattern decomposition, in: E. Prince, J. Stalick (Eds.), Proceedings of the International Conference Accuracy in Powder Diffraction II, NIST Special Publication 846, NIST, Gaithersburg, MD, 1992, pp. 110–126.
[23] J.P. Ramos, A.M.R. Senos, T. Stora, P. Bowen, Master sintering curve determination of nanometric TiC and a TiC-carbon black nanocomposite, to be published.
[24] V. Uvarov, I. Popov, Metrological characterization of X-ray diffraction methods at different acquisition geometries for determination of crystallite size in nano-scale materials, Mater. Charact. 85 (2013) 111–123, https://doi.org/10.1016/j.matchar.2013.09.002.
[25] M.N. Rahaman, Ceramic Processing and Sintering, Marcel Dekker, 2003.
[26] C.C. Koch (Ed.), Nanostructured Materials: Processing, Properties and Potential Applications, 2nd ed., Noyes Publications, New York, 2002.
[27] P. Bowen, C. Carry, From powders to sintered pieces: forming, transformations and sintering of nanostructured ceramic oxides, Powder Technol. 128 (2–3) (2002) 248–255, https://doi.org/10.1016/S0032-5910(02)00183-3.
[28] Outotec Research Center, A. Roine, HSC 7.11 Chemistry Software, (2011) http://www.hsc-chemistry.net/.
[29] H.O. Pierson, Handbook of Refractory Carbides & Nitrides, William Andrew, 1996, https://doi.org/10.1016/B978-081551392-6.50001-5.
[30] E.K. Storms, The Refractory Metal Carbides, Academic Press, New York, 1967.
[31] B. Predel, C-Ti (carbon–titanium), in: B. Predel (Ed.), Landolt-Börnstein – Group IV Physical Chemistry 12B: B–Ba... Cu–Zr, Springer-Verlag Berlin Heidelberg, 2012, pp. 147–149, , https://doi.org/10.1007/978-3-540-44756-6_102.
[32] S. Terashima, The rapid determination of total carbon and sulfur in geological materials by combustion and infrared absorption photometry, Anal. Chim. Acta 101 (1) (1978) 25–31, https://doi.org/10.1016/S0003-2670(01)83836-8.
[33] W. Gruner, Determination of oxygen in oxides by carrier gas hot extraction analysis with simultaneous COx detection, Fresenius' J. Anal. Chem. 365 (7) (1999) 597–603, https://doi.org/10.1007/s002160051529.
[34] J.C. Slater, Atomic radii in crystals, J. Chem. Phys. 41 (10) (1964) 3199, https://doi.org/10.1063/1.1725697.
[35] Y. Li, H. Katsui, T. Goto, Phase decomposition of TiC–ZrC solid solution prepared by spark plasma sintering, Ceram. Int. 41 (10) (2015) 14258–14262, https://doi.org/10.1016/j.ceramint.2015.07.055.
[36] L. Vegard, Die Konstitution der Mischkristalle und die Raumfullung der Atome, Z. Phys. 5 (1) (1921) 17–26, https://doi.org/10.1007/BF01349680.
[37] A. Khorsand Zak, W.A. Majid, M. Abrishami, R. Yousefi, X-ray analysis of ZnO nanoparticles by Williamson–Hall and size–strain plot methods, Solid State Sci. 13 (1) (2011) 251–256, https://doi.org/10.1016/j.solidstatesciences.2010.11.024.